Nanotechnology **18** (2007) 375501 (11pp) doi:10.1088/0957-4484/18/37/375501

Microgrippers: a case study for batch-compatible integration of MEMS with nanostructures

O Sardan[1,4], B Erdem Alaca[1,5], A D Yalcinkaya[1,6], P Bøggild[2], P T Tang[3] and O Hansen[2]

[1] College of Engineering, Koc University, R Feneri Yolu, 34450 Sariyer, Istanbul, Turkey
[2] Department of Micro and Nanotechnology, Danmarks Tekniske Universitet, DK-2800, Kongens Lyngby, Denmark
[3] Department of Manufacturing Engineering and Management, Danmarks Tekniske Universitet, DK-2800, Kongens Lyngby, Denmark

E-mail: ealaca@ku.edu.tr

Received 21 May 2007, in final form 9 July 2007
Published 22 August 2007
Online at stacks.iop.org/Nano/18/375501

Abstract
A batch-compatible integration of micro-electro-mechanical systems (MEMS) with nanoscale objects is demonstrated using the example of a gripping device with nanoscale end-effectors. The proposed nanofabrication technique is based on creating a certain number of nanowires/ribbons on a planar surface, each with a known orientation, using self-assembled crack networks as a template. Since both the location and orientation of the nanowires/ribbons are known, the gripping device can be lithographically transferred on to the substrate ensuring full integration of MEMS with nanoscale end-effectors. Two nanowires/ribbons are attached to each MEMS solely at desired locations with a desired inclination in contrast to most other self-assembly-based techniques of growing nanoscale objects. Challenges unique to MEMS fabrication are encountered raising process requirements beyond those of the simple electrode–nanowire integration. With issues related to yield and end-effector geometry remaining to be studied further, the method proposes a true batch fabrication for nanoscale objects and their integration with MEMS, which does not require the use of nano-lithographic techniques.

(Some figures in this article are in colour only in the electronic version)

1. Introduction

Controlled fabrication of nanostructures itself provides a considerable challenge. When it comes to the integration of these objects with microstructures, especially complex devices rather than simple electrodes, the task becomes even more challenging, with additional process requirements introduced by the existence of microscale components. In this case, the choices regarding precision, speed and the level of investment become highly polarized. On the one hand, top-down techniques such as e-beam lithography and ion-beam milling provide unmatched precision at the expense of parallel processing. On the other hand, bottom-up methods based on self-assembly provide cheaper and faster alternatives, however with much less control on the number and orientation of nanoscale parts. It should be emphasized that without batch compatibility, research in this field remains mainly confined to component development, whereas the leap from components to a full-scale system necessitates further studies on the integration aspect. In the near future, the suitability of a nanofabrication technique for integration with higher-level structures will be considered as vital as its capability of producing well-controlled nanostructures.

[4] Present address: Department of Micro and Nanotechnology, Danmarks Tekniske Universitet, DK-2800, Kongens Lyngby, Denmark.
[5] Author to whom any correspondence should be addressed.
[6] Present address: College of Engineering, Bogazici University, 34342, Bebek, Istanbul, Turkey.

Taking a brief look at the present state of technology, we can conclude that the lack of precision might not constitute a problem in cases where nanoscale objects are grown on a functionalized surface on MEMS with no preference regarding their number and sometimes orientation [1–4]. There are also examples where objects, fabricated elsewhere, are attached on lithographically defined patches by self-assembly [5, 6]. Although high-resolution lithography leads to better spatial control in the latter case, it quickly evolves into a task beyond the capabilities of self-assembly, when it comes to placing a single nanowire at a certain spot on MEMS. Therefore top-down methods, such as e-beam deposition [7, 8] or ion-beam deposition [9], and e-beam lithography [10], remain as preferred tools for integration. Other extreme measures involving advanced manipulation and welding [11–14] are also taken.

To give a more specific example, we can concentrate on the field of material property measurements, which is traditionally concerned with manipulation and integration issues. Considering mechanical measurements first, the majority of tension tests conducted on carbon nanotubes is observed to rely on attaching the nanotube to an atomic force microscope (AFM) tip. Once this step is accomplished, the nanotube is transferred to a MEMS tensilometer [12] or a tension test is carried out with the nanotube spanning two AFM tips [11]. The critical issues associated with both techniques are isolating a single nanotube from the rest and attaching it firmly to the tensilometer or the AFM tips. Such attachment either relies on van der Waals forces [12] or welding of the microstructures with an amorphous carbon film using electron-beam deposition [11, 15].

Similarly, measurement of electrical properties requires physical contact either through nanoscale probes [16] or electrodes. If electrodes are used, various state-of-the-art methods are available: first of all, nanowires can be fabricated together with the electrodes using e-beam lithography [17]. If, instead of e-beam lithography, self-assembly is utilized, there are two possible routes: nanowires are dispersed in a solution and are either attracted towards a substrate using electrostatically [6], chemically [5] and biologically [18] functionalized templates, or external fields for electric [19, 20], magnetic [21] and fluidic [22] assembly are utilized to align the nanowires with respect to electrodes.

In this work, the issue regarding the lack of batch processes for nanoscale patterning is specifically handled within the framework of gripping devices or tweezers, where probes with submicron end-effectors in combination with high-precision motion control are necessary. Therefore tweezers with their stringent precision requirements provide a suitable platform for process and technology development regarding batch compatibility.

Most of the existing nanotweezers are produced by fabricating the actuation mechanism first, and then growing nanoscale extensions either by ion-beam [9, 23] or e-beam [7, 24] deposition. Another approach is based on attaching end-effectors to the microstructure instead of growing them. One such example utilizes nanotube end-effectors attached to the main structure by an amorphous carbon film [25]. In a concept study, an acrylic adhesive was utilized for attaching carbon nanotubes under the view of an optical microscope [26]. And finally, some devices utilize microscale end-effectors which are thinned down to the nanoscale by etching [23].

In contrast to the aforementioned techniques, in this work, end-effectors are fabricated using self-assembled crack networks as a template as explained elsewhere [27, 28]. This process is based on simple photolithography instead of sophisticated, serial techniques. Although the cracks or templates are formed by self-assembly, the technique provides end-effectors with predetermined numbers and orientations. Hence, this nanofabrication step may be followed by the fabrication of microscale electrostatic actuators with full registry and perfect alignment between two steps leading to a successful integration. It is claimed that, compared to electric, magnetic or fluidic field-assisted assembly, chemical vapor deposition (CVD)-based growth techniques or techniques based on surface functionalization, the proposed method provides an elegant way of placing a nanowire at a desired spot with a desired inclination with respect to the main structure. In the remainder of the paper, a discussion on the actuator design and analysis will be followed by fabrication details. The paper will be concluded with integration results.

2. Design of electrostatic actuators

An electrostatic comb-drive actuator with double-folded beam flexures is chosen as the movement device for the microgripper (figure 1). A potential difference between the movable and fixed comb structures creates an electrostatic force due to the capacitive energy stored in the system. The simplest symmetrical design for the electrostatically actuated microgripper is composed of three combs, as shown in figure 1(a). The comb in the middle is fixed. The combs on both sides are anchored to the substrate via double-folded cantilever flexures, and hence, they are movable. Gripping action, i.e. closing the gripping ends, can be achieved by applying a voltage to the comb in the middle and grounding the movable ones. However, due to the fact that electrostatic forces are always attractive, motion in the opposite direction is not possible with this configuration. Controlled opening of gripping ends would become possible with the addition of two fixed combs on the exterior side of both movable combs [29], which is not pursued in this study. In this section, comb-drive and flexure design will be explained and the final list of design parameters will be given.

2.1. Design of comb-drives

The total capacitance between a certain number of pairs of interdigitated comb fingers (figure 2) can be written as the sum of the capacitances due to interaction of the lateral and longitudinal comb faces as

$$C_{\text{total}} = C_x + C_y = 2N_{\text{f}}\varepsilon_0 h\left(\frac{w}{g_x - x} + \frac{t + x}{g_y}\right), \quad (1)$$

where N_{f} is the number of comb fingers on each comb, h is height of the device, w is width of each comb finger, t is the zero voltage overlap length between the fingers, g_x and g_y are the gap distances in the x- and y-directions, respectively, x is

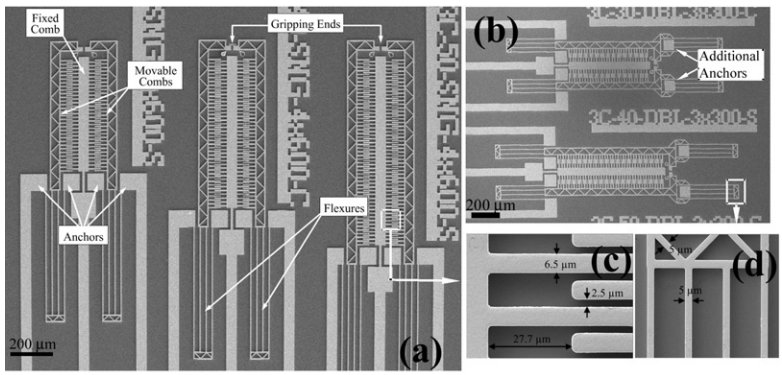

Figure 1. (a) Scanning electron micrograph showing the basic components of three different microgrippers. (b) A three-comb structure anchored at both ends. (c) Detailed view of comb fingers. (d) Detailed view of double-folded cantilever flexures.

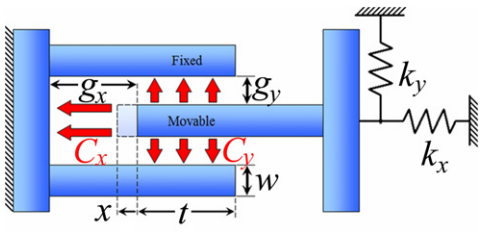

Figure 2. Schematic illustration of a close-up view of a single pair of interdigitated comb fingers.

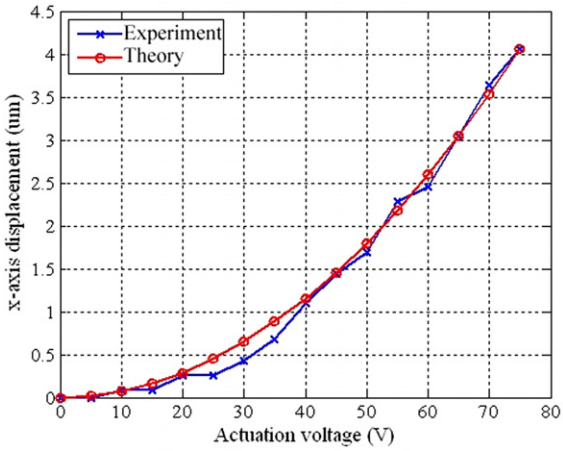

Figure 3. Displacement versus drive voltage characteristics of the electrostatic comb-drive actuator for the following parameters: *number of fingers* = 50, *finger gap* = 4 μm (design parameter), 3.9 μm (measured), *spring height* = 7 μm (design parameter), 6 μm (measured), *spring length* = 400 μm (design parameter, measured), *spring width* = 4 μm (design parameter), 3.65 μm (measured). The theoretical curve was drawn considering the actual dimensions of the electrostatic actuator instead of the design parameters.

the displacement in x-direction and $\varepsilon_0 = 8.85 \times 10^{-12}$ F m^{-1} is the permittivity of free space [30].

The capacitive energy stored due to a voltage difference, V, between two combs is $W_{es} = C_{tot}V^2/2$. The electrostatic force is then obtained by taking the derivative of the energy expression with respect to the displacement in the x-direction, $F_{es} = -\partial W_{es}/\partial x$, leading to the following equation [30]:

$$F_{es} = -N_f \varepsilon_0 h \left(\frac{w}{(g_x - x)^2} + \frac{1}{g_y} \right) V^2. \qquad (2)$$

In the small-signal regime, where a linear behavior of the springs is assumed, the displacement, x, can be determined according to Hooke's Law as

$$x = F_{es}/k_{mech,x}. \qquad (3)$$

As can be seen from equations (2) and (3), the actuator displacement has a quadratic dependence on the drive voltage due to the nonlinear nature of the electrostatic force. This is experimentally verified in figure 3, where the theoretical calculation relying on equations (2) and (3) is overlaid on the DC deflection measurements for a specific design, as explained in the caption.

2.2. Design of flexures

A double-folded cantilever beam is a parallel combination of two folded cantilever beam structures. Taking equal lengths for both beams, the mechanical spring constants in the x-direction and the z-direction (out-of-plane), $k_{mech,x}$ and $k_{mech,z}$, respectively, are calculated as

$$k_{mech,x} = \frac{E h_s w_s^3}{l_s^3} \quad \text{and} \quad k_{mech,z} = \frac{E h_s^3 w_s}{l_s^3}, \qquad (4)$$

where E is the modulus of elasticity ($E = 204$ GPa for nickel), h_s is the height of the spring (the same as the device height, h, mentioned above), w_s is the width of the spring, and l_s is the length of the cantilever beams of the structure [31].

The devices anchored at both ends (figure 1(b)) lead to a more stable operation and better levitation control. The overall spring constant for such devices in the movement direction is $2k_{mech,x}$.

2.3. Parameter selection

Devices with various actuation mechanisms having different comb-drive and spring configurations or different dimensions

Table 1. Comb-drive design parameters.

		Designed	Fabricated
Number of comb fingers	N_f	30, 40 or 50	
Device height	h	7 μm	5–6 μm
Zero voltage overlap	t	30 μm	30–32.5 μm
Longitudinal gap distance	g_x	30 μm	27.5–30 μm
Lateral gap distance	g_y	4 μm	2.5–4 μm

Table 2. Flexure design parameters.

		Designed	Fabricated
Spring height	h_s	7 μm	5–6 μm
Spring width	w_s	3 or 4 μm	3.5–5 μm
Cantilever beam length	l_s	300, 400, 500 or 600 μm	

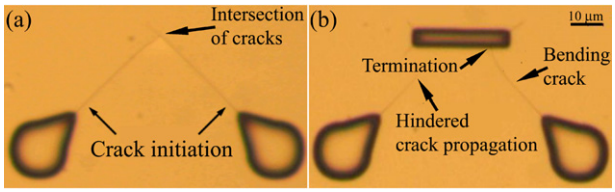

Figure 4. Two different configurations employed in this study. (a) Two 10 μm deep crack initiation patterns (etched using a standard DRIE recipe) with no crack termination feature. The cracks intersect in the middle, and hence, resulting nanoscale end-effectors will be connected. (b) Two crack initiation patterns with a crack termination feature. The cracks are attracted towards the crack termination site which is apparent in the bending of the right crack. The crack on the left-hand side did not propagate all the way to the termination site. Note that edges of the termination feature initiated unwanted cracks. This effect can be suppressed by rounding the corners [27].

were fabricated. Due to the fact that the gripping range for the microgripper is of the order of a few micrometers and considering operational requirements together with possible restrictions due to fabrication processes, the design parameters in tables 1 and 2 were chosen for comb-drives and double-folded cantilever flexures. The resulting variations are also listed.

Electrostatic pull-in analysis and mechanical stability analysis (for both lateral and out-of-plane motion cases) were carried out individually for all devices with different design parameters. The results indicate that all designs are valid and that devices with different dimensions can be operated properly by varying the applied voltage.

3. Fabrication

3.1. Fabrication philosophy

The first stage in fabrication is the deposition of nanoscale end-effectors on a Si substrate. These structures are in the form of nanoribbons or nanowires starting and terminating at lithographically defined points, and they remain attached to Si along their entire length. Although they resemble planar structures that are electrodeposited in PMMA molds created by electron-beam lithography, they are in fact quite different. They are obtained by filling cracks in a sacrificial SiO_2 coating on Si [27, 28]. In contrast to electron-beam lithography and other serial fabrication methods, the patterning capability makes this technique batch compatible, where the initiation and termination spots of cracks are created by photolithography, and the crack formation occurs simultaneously on the wafer level. Filling of cracks on other thin film/substrate systems is also reported [32]. Combined with thin-film delamination, the technique is also demonstrated to facilitate the implementation of shadow masking at the nanoscale [33].

The process starts by depositing a SiO_2 film with a modified chemistry using plasma-enhanced chemical vapor deposition (PECVD). It is observed that in the presence of excess nitrous oxide, silanol (Si–OH) incorporation takes place leading to the formation of $SiO_{3/2}OH$ instead of SiO_2 [34]. Annealing of the deposited film results in a condensation reaction and a volumetric shrinkage. Due to the constraint provided by the substrate, this, in turn, leads to the development of tensile stresses, which are proportional to the concentration of evolved hydrogen [35]. These thermally induced stresses are responsible for cracking.

Along the thickness direction, cracks are observed to propagate through the oxide coating and arrest at the Si interface [27]. In the plane of the substrate, however, their propagation direction is dictated by the crystalline anisotropy of Si. They propagate along the ⟨100⟩ directions of the (100) Si substrate due to the diminished elastic modulus and decreased resistance to crack opening [28]. However, a certain distribution of mechanical stresses in SiO_2 under loading can be achieved to eliminate this effect. Patterning of the Si substrate is demonstrated to be an efficient way of dictating stresses, where sharp corners are used to amplify stresses and initiate cracks, and free edges provide traction-free zones toward which cracks are attracted. The stress amplification is found to be due to the creation of sharp wedges during nonconformal deposition of oxide film as explained elsewhere [36]. Therefore, when the SiO_2 coating is subjected to thermal loading, a crack network self-assembles, whose pattern is solely determined by the initial distribution of crack initiators and terminators. Specific configurations employed in this study are shown in figure 4.

After the cracks are filled with the material of choice and the end-effectors thus are obtained, the fabrication of the microscale actuation mechanism is carried out as the second step. Since the location and orientation of each end-effector is known, the integration of the microscale device with nanoscale extensions is realized within the boundaries of simple photolithography. Once the integration is accomplished and end-effectors are securely attached to the device, the movable parts are released from the substrate, and the device is finished.

This alignment approach is essentially not very different from, for example, dielectrophoresis, where one-dimensional structures are polarized and moved in an external electric field and assemble with respect to pre-patterned electrodes. In our case, we have a mechanical stress field in the silicon dioxide coating that determines the assembly of the cracks with respect to crack initiators and terminators with a much better control on spatial density and orientation.

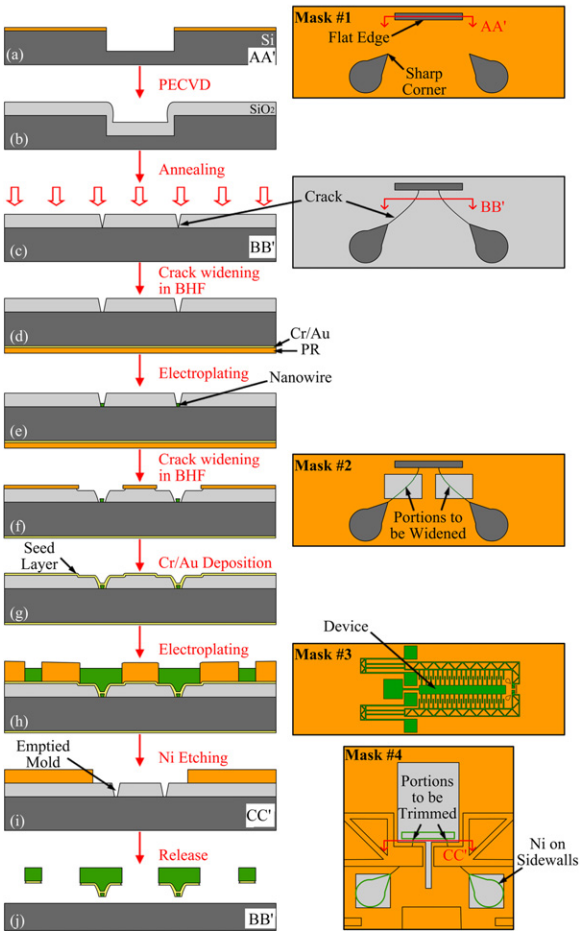

Figure 5. The basic fabrication sequence.

3.2. *Fabrication process*

The fabrication process for the electrostatically actuated microgrippers, illustrated in figure 5, starts with a low-resistivity (<0.0025 Ω cm) (100) silicon wafer, which is 500–550 μm thick and 4 inches in diameter.

3.2.1. Crack initiator etching. The first step is etching of triangles with sharp edges or trenches with free surfaces into the Si substrate via inductively coupled plasma deep-reactive ion etching (ICP-DRIE) using Mask#1 (figure 5(a)). An optimization study was carried out to find the best combination of etch power and resist thickness to retain the sharpness of the crack initiators; otherwise crack initiation could be inhibited (see figure 4). High radio frequency (RF) power during etching was required to enhance the etch anisotropy, whereas a low resist thickness is necessary for the precision of the pattern transfer. The minimum resist thickness that would survive high-power DRIE and still lead to a reasonable etch depth was determined to be 1.5 μm. The etch rate of the high-power DRIE recipe turned out to be 0.93 μm min^{-1}, and an etch depth of 6.5 μm obtained through a 6 min etch was observed to be sufficient for crack initiation.

3.2.2. Nanoscale end-effector fabrication. Once the substrate was patterned with crack initiators and terminators, a 4.6 μm thick layer of sacrificial SiO_2 film with modified chemistry was blanket-deposited using PECVD (figure 5(b)). The deposition parameters are reported elsewhere [27, 28].

Upon annealing at 500 °C for 40 min, a crack network was obtained in the SiO_2 coating with the cracks terminating at the Si/SiO_2 interface. (figure 5(c)). It should be emphasized that cracks form and propagate along the line of symmetry of the crack initiating features as shown in figure 4. Hence, the relative orientation and position of a crack pair is fixed. This makes the use of a standard mask aligner possible during all lithography steps with an alignment tolerance on the order of 1 μm depending on the quality of the alignment mark design and operator skills.

The cracks were then ready to be utilized as molds during electroplating of nanoscale end-effectors where deposition takes place on the low-resistivity Si interface at the crack tip leaving the SiO_2 surface intact. The fact that electrodeposition is to occur directly on the Si substrate in the absence of any seed layers should also be emphasized at this point to highlight the difficulty associated with the process. In order to achieve a uniform electric field distribution through low substrate resistance during electroplating, a thin layer of chromium and gold (10 nm and 200 nm, respectively) was deposited on the back surface of the wafer, which was then covered with a 2.2 μm thick photoresist film to prevent any deposition here. An opening should be left on the resist close to the wafer edge for electrical contact. Moreover, since the opening at the Si/SiO_2 interface was on the order of only a few nanometers, the cracks were widened slightly by etching in buffered hydrofluoric acid (BHF) just before electroplating (figure 5(d)). Note that the width of the resulting nanowires is determined by the etch time at this step. In order to eliminate the formation of any native oxide on the Si surface, either the electroplating step should be carried immediately after the BHF etch or the wafer should be dipped into a diluted acid bath for just a few seconds prior to nanowire deposition.

Nanoscale end-effectors were then deposited inside these widened cracks using a nickel electroplating bath [37]. It should be kept in mind that side walls and bottom of crack initiation grooves are not fully covered by the sacrificial SiO_2 layer. Consequently, it is not possible to calculate the effective plating area for nanowire deposition exactly; thus, the optimal plating current cannot be determined, and this requires further process optimization for both the deposition rate and the surface quality of the resulting nanowires.

The wafer was clamped to a single-contact wafer holder at the location where Cr/Au layer was exposed on the back. After dipping the wafer into the electrolyte solution, the wafer holder was electrically connected to the anode and the current was gradually increased to 160 mA. Hence, Ni deposition started on the wafer surface inside the crack molds forming nanowires (figure 5(e)). In order to enhance the uniformity over the wafer, the electrolyte solution was agitated by purging compressed air through a number of holes in a tube at the bottom of the tank. After 35 s, which corresponds to a deposition thickness on the order of 500 nm, the current was gradually decreased to zero and the wafer was taken out of the plating bath. After rinsing the wafer in deionized (DI) water for 2 min, the photoresist layer at the back was removed in acetone and the rinsing step was repeated one more time.

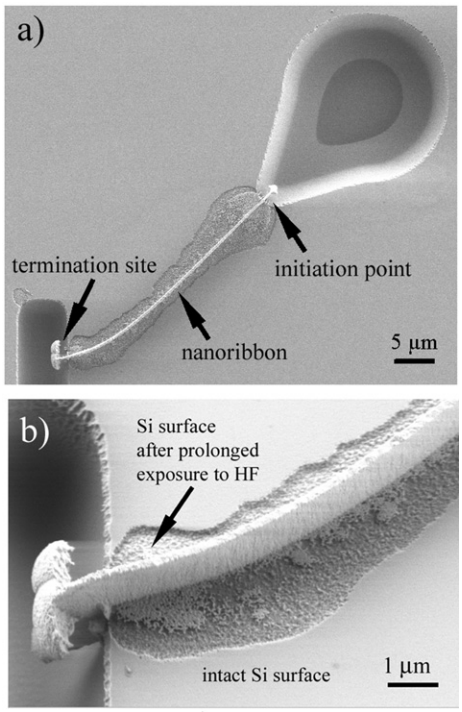

Figure 6. SEM images showing (a) top view of a bent nanoribbon and (b) 45° tilted view of the nanoribbon end as a result of a 1 min Ni deposition performed at 40 mA. Note that to reveal the nanoribbon buried inside the crack, the sacrificial oxide layer was removed by wet etching. During this process, Si in the immediate vicinity was exposed to BHF along the Si/SiO_2 interface.

It should be emphasized that widthwise, the resulting end-effectors are confined within the cracks, whose opening is determined during the initial BHF step. Their thickness, on the other hand, is a function of the deposition time. Longer deposition times lead to planar structures, such as the nanoribbon of figure 6 obtained after 1 min of deposition. Other types of resulting end-effectors will be presented in the following sections.

3.2.3. Preparation of the seed layer for nano–micro integration. Since the sacrificial SiO_2 layer is not electrically conductive, it is necessary to deposit a plating base prior to the electrodeposition of the actuator. Electroplating of the actuator will also take place on top of the nanoscale end-effectors, where these will be attached to the actuator. The strength of this bond is critical for device performance. Therefore it is important to further widen the crack opening in this integration zone to allow the plating base to reach into cracks in physical vapor deposition. The widening was carried out using wet etching in BHF. The remaining SiO_2 layer was protected using Mask#2 (figure 5(f)). A micrograph of the process is shown in figure 7.

Following the removal of the photoresist mask in acetone and rinsing of the wafer in DI water for 2 min, a 10 nm/200 nm Cr/Au layer was deposited on the front side of the wafer by e-beam evaporation (figure 5(g)). This provides the connection between the nanoscale end-effectors and the actuator devices and also serves as a plating base for actuator deposition.

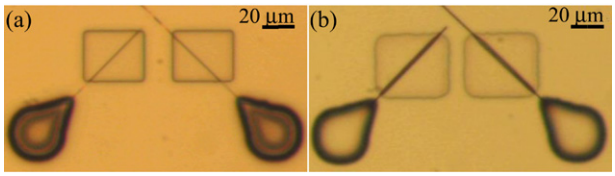

Figure 7. Optical microscope image of (a) a crack pair with Mask#2 applied and (b) a similar crack pair after a 5 min BHF etch and removal of Mask#2.

3.2.4. Actuator fabrication. After seed layer deposition, a 9.5 μm thick photoresist film was spun on the wafer and patterned using Mask#3. Hence, a mold defining the actuator devices was prepared. The best resolution achieved at this lithography step was about 2 μm for both positive and negative patterns. Square-shaped platforms at the tip of the MEMS actuator are designed to compensate this misalignment. This, combined with a careful design of the nanowire cutting mask (Mask#4), ensures a working pair of tweezers.

The wafer was then clamped to a three-contact wafer holder. Electrical connection to the Cr/Au plating base was then achieved through openings in the resist layer. The electrodeposition was performed using a Ni electroplating bath [37] (figure 5(h)). The procedure was similar to the case of end-effector fabrication. After dipping the wafer into the electrolyte solution, the wafer holder was electrically connected to the anode and the current was gradually increased to 250 mA. Ni deposition started on the Cr/Au seed layer inside the photoresist mold, forming device structures. The electrolyte solution was agitated by air bubbles. Uniformity at the edges was further enhanced by using a current thief, i.e. connecting a dummy electrode in the form of a ring surrounding the wafer to a secondary cathode [37]. The expected deposition rate for Ni was 0.2 μm min^{-1} at 1.0 A dm^{-2} and the process parameters corresponded to a device thickness of 6 μm for the active electroplating area defined by Mask#3. After 30 min of deposition, the current was decreased to zero and the wafer was taken out of the plating bath. Finally, after rinsing the wafer in DI water for 2 min, the 9.5 μm thick photoresist layer on the front was removed in acetone and the rinsing step was repeated one more time.

The variation of actual dimensions was already given in tables 1 and 2. Considering a three-comb single anchored device as an example (figure 1(a)), the thickness of the comb fingers, which were designed as 5 μm, came out to be 6.5 μm, resulting in a lateral gap of 2.5 μm instead of 4 μm (figure 1(c)). Similarly, this enlargement of dimensions also led to a longitudinal gap of 27.7 μm rather than 30 μm. The thickness of the double-folded cantilever flexures for the same device turned out to be 5 μm instead of 4 μm (figure 1(d)).

Considering a double-anchored device at a different location on the same wafer (figure 1(b)), it was observed that even though dimensions of the fabricated device were closer to the design parameters than the previous case, the edges of both comb fingers and device tips were rounded. However, this effect is not expected to influence significantly either the electrostatic behavior or proper operation of the device.

At this stage, the movable combs are connected to each other through intersecting nanoribbon end-effectors, as shown in figure 8.

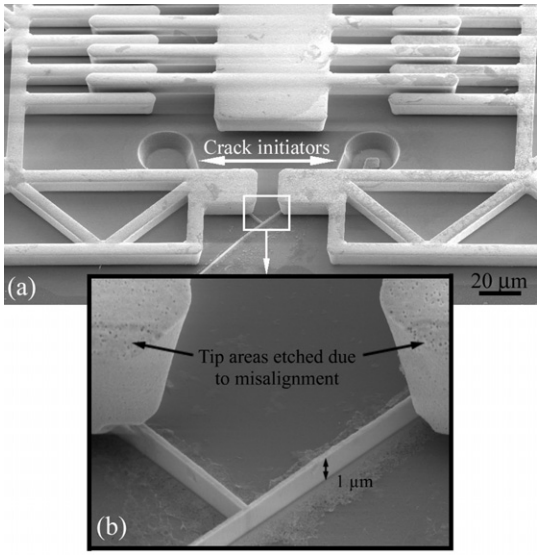

Figure 8. (a) SEM image showing a 45° tilted front view of a microgripper after etching of the sacrificial SiO_2 layer. (b) Merged nanoribbon end-effectors in detail.

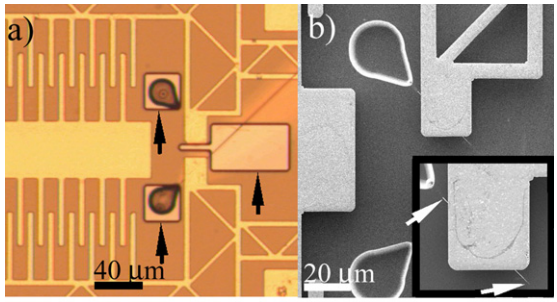

Figure 9. (a) Regions designated with arrows are exposed to the Ni etchant; hence, the nanowires are freed from initiation and termination locations. Note the slight upwards shift of Mask#4 with respect to the device, which leads to a slight etching of the device tips. Furthermore, only the lower crack initiator successfully produced a nanowire. It should be noted that the visible line is the crack with the end-effector buried inside. (b) SEM image showing the tip of the microgripper after etching of the sacrificial SiO_2 layer with the inset showing the single nanowire end-effector successfully detached from both ends after the Ni etch.

3.2.5. Cutting of nanowire ends. The last step before the release process was separating the end-effectors from crack initiation and termination sites and cutting them to a desired length. In order to expose the desired portions of end-effectors to a Ni etchant, the Cr/Au seed layer covering the wafer surface, including both the sacrificial SiO_2 layer and the end-effectors, should be removed. The 200 nm thick Au layer was removed first in Entreat 100 (trademark of Engelhard Company) for 18 min and the wafer was rinsed in DI water for 5 min. Entreat 100 is an ideal Au etchant providing good selectivity over Ni. Etching was followed by the removal of the 10 nm thick Cr layer in a commercial Cr etchant for 40 s. Since the Cr etchant attacks Ni with a relatively low etch rate, and the etch time was quite short, the Ni structures were not damaged. Overetch should be prevented in both Au and Cr etch steps in order for the end-effectors to remain attached to device tips and for the devices to remain anchored on the substrate.

After Au and Cr removal, the Ni end-effectors were cut to the desired length by etching in a 13% (w/w) solution of nitric acid (HNO_3) for $6\frac{1}{2}$ min using a 6.2 μm thick photoresist mask patterned with Mask#4 (figure 5(i)). This mask exposes the portions of the nanoscale end-effectors to be cut and Ni deposited on the side walls of crack initiators and terminators, if used. Figure 9(a) shows one such configuration where the exposed regions are evident. Hence, the length of the protruding end-effectors was determined at this stage. Considering the possibility of a misalignment between lithography steps and anomalous crack formation, the exposed area was extended into the region between the square-shaped platforms. However, due to satisfactory mask alignment and crack formation, this feature was never utilized. When the wafers were investigated after release, it was observed that nanoribbon end-effectors were successfully detached from both their intersecting counterparts and the excess Ni deposited on crack inducer walls (figure 9(b)).

The wafer was then rinsed in DI water for 2 min. Finally, after the 6.2 μm thick photoresist layer on the front was removed in acetone and rinsing step was repeated, the devices were ready to be released.

3.2.6. Release. The last step in the fabrication of the electrostatically actuated microgrippers is the release of the devices (figure 5(j)). For this purpose, the sacrificial SiO_2 layer was removed from beneath the movable combs by wet etching in BHF for 24 min. This is the first step where end-effectors, otherwise buried inside the oxide layer, become visible under the microscope.

Since nanoscale end-effectors were still attached to the Si substrate, the substrate was etched using a 33 wt% KOH solution at 60 °C. This resulted in an etch rate of 0.54 μm min^{-1}, and a 10 min etch time was found to be sufficient to produce functional devices. In order to reduce sticking of the released devices to the substrate surface due to the ubiquitous capillary forces, the devices were dried in ethanol vapor at 72 °C after DI water rinse. Released actuators and nanoribbons are shown in figure 10.

To check whether nano- and microcomponents kept their integrity during release, we conducted two separate tests. First of all, a nanoribbon was pushed by a silica probe under the view of an optical microscope. The resulting deformation is shown in figure 11. It was observed that the nanoribbon could be bent by almost 70° without any fracture occurring in the ribbon or along its interface with the microstructure. When the loading was removed, the nanoribbon was observed to spring back to its original position, indicating complete elasticity.

It should be noted that the end-effector was loaded very close to its base rather than at the free end. If one applies the load at the free end, a much lower load would be sufficient to deflect the structure by a given amount. If, however, the point of the application of load is receded toward the base, the amount of required load to obtain the same deflection increases. The portion of the end-effector between the base and the point of application of the load is then subjected to higher bending stresses, whereas the rest of the structure remains stress-free. In a linear elastic regime, one needs to increase the load 69 times compared to the free-end loading, if the distance

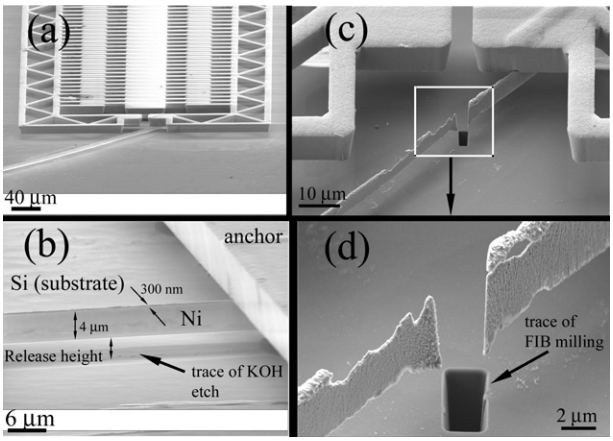

Figure 10. (a) Front view of the microgripper with nanoscale end-effectors in the form of ribbons after complete release. (b) A detailed view of a released ribbon. (c) A view of the gripping end of the tweezers. In this particular case, the end-effector is cut by focused ion beam (FIB). FIB-induced changes are evident when the detailed view in (d) is compared with the intact nanoribbon of (b).

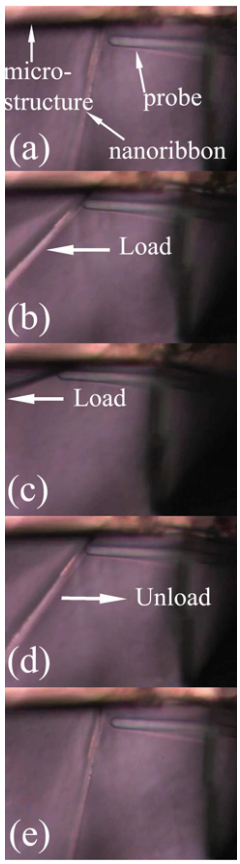

Figure 11. A sequence showing the loading and unloading of a nanoribbon by the motion of an external probe. The ribbon is bent by almost 70°. Neither the ribbon nor its attachment to the microstructure failed during loading. Upon unloading, the nanoribbon returned to its original position, indicating complete elasticity. Horizontal arrows in (b)–(d) indicate the direction of (un)loading.

between the base and the point of load application is reduced to one tenth of the length of the structure.

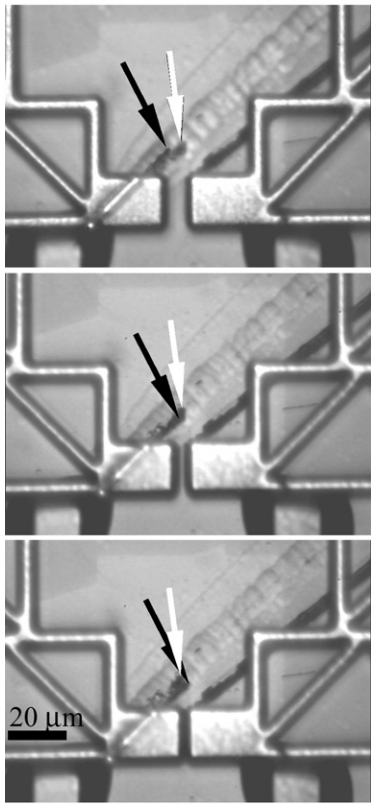

Figure 12. A sequence of optical micrographs showing the closing of the tweezers. The same actuator as that shown in figures 10(c) and (d) is utilized. The end of the nanoribbon attached to the left platform is designated with a dark arrow. The white arrow points on to the stationary trench milled in the Si substrate by FIB. The experiment demonstrates that the nanoribbon and the microactuator act as a single entity.

The survival of the structure under these conditions is due to the specific sulphamate nickel bath used for electroplating. The bath is optimized to have low internal stresses using a low deposition temperature and a low deposition rate. The bath contains various grain refining additives making a grain size around 50 nm possible. This is the main reason for the relatively high hardness of 440 HV (under 50 g load) as opposed to 210 HV for conventional sulphamate nickel [38]. This corresponds to a tensile strength of 1300 MPa [39].

This experiment also verifies that the nanowires are well attached to the device and probably withstand any forces required to pick up objects which are not attached to the substrate surface, e.g. latex beads of 1–5 μm diameter. The lateral stiffness of a 2 μm long end-effector with a 300 nm width and a 4 μm height can be calculated as 688.5 N m^{-1}, which can considered to be sufficiently high. However, bending of the nanowires becomes an issue if samples attached to the substrate surface are to be manipulated, e.g. PECVD-grown carbon nanotubes.

The particular actuator with a single nanoribbon extension shown in figures 10(c) and (d) is then utilized in the experiment of figure 12. Here the left-hand comb is brought slowly toward the stationary comb and the resulting motion is captured under an optical microscope. The trench in the Si substrate produced by FIB milling is used as a reference point (designated with

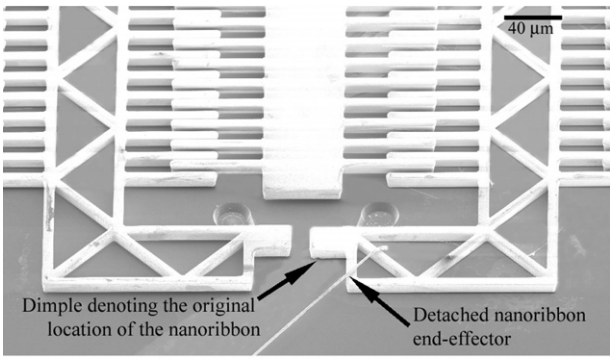

Figure 13. SEM image showing 45° tilted front view of the microgripper with a detached end-effector.

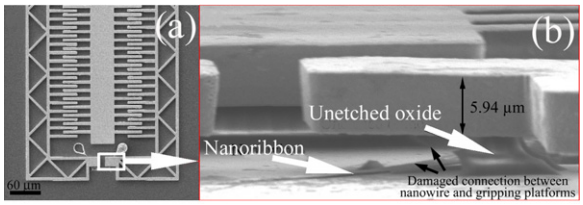

Figure 14. (a) Top-view of the device and (b) a tilted SEM image showing the broken connection between the end-effector and the device underneath the square-shaped gripping platform. Due to insufficient crack widening (figure 7) prior to actuator fabrication, the connections between actuators and end-effectors were formed as high-aspect-ratio structures prone to failure during release.

the white arrow) and the motion of the tip of the nanoribbon is traced by the dark arrow. It is evident that the end-effector moves together with the device tip.

3.3. Fabrication issues

Two main issues are observed to remain for further study.

(1) *The yield related to end-effector fabrication.* Most of the microgrippers are observed to have only a single end-effector. Although better yield was obtained with the same method previously [28], various etching and deposition steps involved in the actuator fabrication are responsible for missing end-effectors. For example, figure 13 shows a failed device where the end-effector is detached from the device during the removal of the oxide mold. This can be prevented by etching more oxide from the square-shaped openings in figure 7 using Mask#2. This will increase the contact area between the nanowire and the device as opposed to the weak chimney (figure 14) that does not provide enough support and is prone to failure under various loadings created in wet etching.

(2) *End-effector geometry.* The width of the end-effectors is governed by the crack width, which is a function of BHF etch time prior to nanowire deposition. Interested readers are referred to [28] for a discussion on the fundamental limits of the nanowire thickness. The height, on the other hand, merely depends on deposition time. Hence, one can control the end-effector dimensions by changing these two parameters. In this study, however, a variety of geometries are observed. Some end-effectors turned out to be nanoribbons with a width of 300 nm (figures 6 and 8), whereas others are observed to resemble bigger ribbons, again with a width of 300 nm, but with a considerable height of 4 μm, as shown in figures 10(b) and (d). The reason for such structures with an aspect ratio larger than ten is likely to be the inadequate masking of nanotemplates during the electrodeposition of the devices. Hence, unprotected, 5 μm deep templates, originally with a nanowire at the bottom, are filled with Ni up to an increased height, whereas the width of 300 nm is preserved due to the geometric constraint imposed by the template width. To prevent this unwanted secondary growth within the templates, square-shaped platforms at the device tip, over which the integration with end-effectors takes place, should be kept smaller than the actual square-shaped openings on the substrate. The surrounding photoresist will mask crack openings at the corner and prevent further deposition of Ni within the cracks as shown in figure 15.

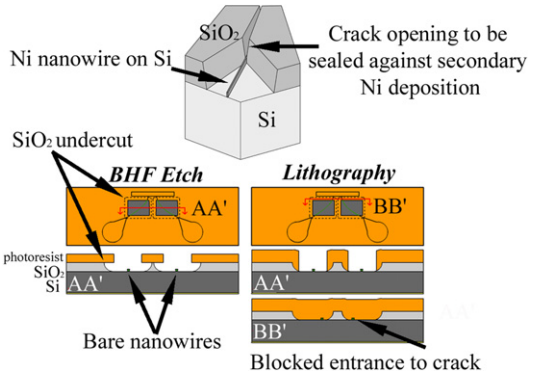

Figure 15. An initial BHF etch leads to a considerable undercut in the oxide layer and crack widening. A lithography step can then be employed to block the entrance of the crack to electroplating solution and prevent the unwanted secondary deposition of Ni into the cracks during device fabrication.

4. Conclusion

A case study for a batch-compatible integration concept of MEMS with nanoscale objects is presented in the form of microgrippers with submicron to nanoscale end-effectors. As opposed to the usual routes taken during the fabrication of such devices, the devices are fabricated using a directed self-assembly method, which first leads to a well-defined distribution of nanoscale objects on the substrate. Since this distribution is governed by features created by conventional photolithography, nanoscale objects are automatically aligned with respect to subsequent layers. The nanofabrication step is then followed by the microfabrication of the rest of the structures. We have demonstrated the successful integration of MEMS devices and nanostructures.

However, some issues remain for further study. For example, most of the devices are observed to include only one end-effector as opposed to two as originally designed. This is a yield question that needs to be addressed in more detail.

Furthermore, depending on the specific batch, some of the end-effectors are observed to be in the form of nanoribbons with a width of 300 nm, while others form even larger ribbons which are 300 nm in width and 4 μm in height. The appearance of such structures is related to the fact that the templates could not be protected during additional electrodeposition steps, and hence, the end-effectors, originally in the form of nanowires, grow in height whereas their width is preserved due to the constraints imposed by the geometry of the templates. We note that these unusual knife-shaped structures may have applications, in particular, if the dimensions can be tuned further. These difficulties highlight challenges for process development for MEMS integration due to multiple mask usage and topography-related requirements as opposed to simple electrode–nanowire integration studies.

Acknowledgments

BEA acknowledges support by Tübitak under Grant No. 104M216. We thank Danchip staff for their assistance with process details.

References

[1] Islam M S, Sharma S, Kamins T I and Williams R S 2004 Ultrahigh-density silicon nanobridges formed between two vertical silicon surfaces *Nanotechnology* **15** L5–8

[2] Englander O, Christensen D, Kim J, Lin L and Morris S J S 2005 Electric-field assisted growth and self-assembly of intrinsic silicon nanowires *Nano Lett.* **5** 705–8

[3] Northen M T and Turner K L 2006 Meso-scale adhesion testing of integrated micro-and nano-scale structures *Sensors Actuators* A **130/131** 583–7

[4] Jungen A, Stampfer C, Hoetzel J, Bright V M and Hierold C 2006 Process integration of carbon nanotubes into microelectromechanical systems *Sensors Actuators* A **130/131** 588–94

[5] Liu J, Casavant M J, Cox M, Walters D A, Boul P, Lu W, Rimberg A J, Smith K A, Colbert D T and Smalley R E 1999 Controlled deposition of individual single-walled carbon nanotubes on chemically functionalized templates *Chem. Phys. Lett.* **303** 125–9

[6] Myung S, Lee M, Kim G T, Ha J S and Hong S 2005 Large-scale surface-programmed assembly of pristine vanadium oxide nanowire-based devices *Adv. Mater.* **17** 2361–4

[7] Bøggild P, Hansen T M, Tanasa C and Grey F 2001 Fabrication and actuation of customized nanotweezers with a 25 nm gap *Nanotechnology* **12** 331–5

[8] Mølhave K, Madsen D N, Rasmussen A M, Carlson A, Appel C C, Brorson M, Jacobsen J H and Bøggild P 2003 Solid gold nanostructures fabricated by electron beam deposition *Nano Lett.* **3** 1499–503

[9] Kometani R *et al* 2004 Nanomanipulator and actuator fabrication on glass capillary by focused-ion-beam-chemical vapor deposition *J. Vac. Sci. Technol.* B **22** 257–63

[10] Yun M, Myung N V, Vasquez R P, Lee C, Menke E and Penner R M 2004 Electrochemically grown wires for individually addressable sensor arrays *Nano Lett.* **4** 419–22

[11] Akita S, Nishijima H, Nakayama Y, Tokumasu F and Takeyasu K 1999 Carbon nanotube tips for a scanning probe microscope: their fabrication and properties *J. Phys. D: Appl. Phys.* **32** 1044–8

[12] Williams P A, Papadakis S J, Falvo M R, Patel A M, Sinclair M, Seeger A, Helser A, Taylor R M II, Washburn S and Superfine R 2002 Controlled placement of an individual carbon nanotube onto a microelectromechanical structure *Appl. Phys. Lett.* **80** 2574–6

[13] Kim K S, Lim S C, Lee I B, An K H, Bae D J, Choi S, Yoo J-E and Lee Y H 2003 *Insitu* manipulation and characterizations using nanomanipulators inside a field emission-scanning electron microscope *Rev. Sci. Instrum.* **74** 4021–5

[14] Chen C, Yan L, Kong E S-W and Zhang Y 2006 Ultrasonic nanowelding of carbon nanotubes to metal electrodes *Nanotechnology* **17** 2192–7

[15] Yu M-F, Lourie O, Dyer M J, Moloni K, Kelly T F and Ruoff R S 2000 Strength and breaking mechanism of multiwalled carbon nanotubes under tensile load *Science* **287** 637–40

[16] Zach M P, Ng K H and Penner R M 2000 Molybdenum nanowires by electrodeposition *Science* **290** 2120–3

[17] Tilke A T, Simmel F C, Lorenz H, Blick R H and Kotthaus J P 2003 Quantum interference in a one-dimensional silicon nanowire *Phys. Rev.* B **68** 075311

[18] Kovtyukhova N I and Mallouk T E 2002 Nanowires as building blocks for self-assembling logic and memory circuits *Chem. Eur. J.* **8** 4355–63

[19] Smith P A, Nordquist C D, Jackson T N and Mayer T S 2000 Electric-field assisted assembly and alignment of metallic nanowires *Appl. Phys. Lett.* **77** 1399–401

[20] Narayanan A, Dan Y, Deshpande V, Lello N D, Evoy S and Raman S 2006 Dielectrophoretic integration of nanodevices with CMOS VLSI circuitry *IEEE Trans. Nanotechnol.* **5** 101–9

[21] Hangarter C M and Myung N V 2005 Magnetic alignment of nanowires *Chem. Mater.* **17** 1320–4

[22] Huang Y, Duan X, Wei Q and Lieber C M 2001 Directed assembly of one-dimensional nanostructures into functional networks *Science* **291** 630–3

[23] Wang X, Vincent L, Yu M, Huang Y and Liu C 2003 Architecture of a three-probe MEMS nanomanipulator with nanoscale end-effectors *Proc. IEEE/ASME Int. Conf. on Advanced Intelligent Mechatronics (Kobe)* pp 891–6

[24] Ooi T, Matsumoto K, Nakao M, Otsubo M, Shirakata S, Tanaka S and Hatamura Y 2000 3D nano wire-frame for handling and observing a single DNA fiber *Proc. 13th Annu. Int. Conf. on Micro Electro Mechanical Systems (Miyazaki)* pp 580–3

[25] Nakayama Y 2002 Scanning probe microscopy installed with nanotube probes and nanotube tweezers *Ultramicroscopy* **91** 49–56

[26] Kim P and Lieber C M 1999 Nanotube nanotweezers *Science* **286** 2148–50

[27] Alaca B E, Sehitoglu H and Saif T 2004 Guided self-assembly of metallic nanowires and channels *Appl. Phys. Lett.* **84** 4669–71

[28] Sardan O, Yalcinkaya A D and Alaca B E 2006 Self-assembly-based batch fabrication of nickel–iron nanowires by electroplating *Nanotechnology* **17** 2227–33

[29] Mølhave K, Hansen T M, Madsen D N and Bøggild P 2004 Towards pick-and-place assembly of nanostructures *J. Nanosci. Nanotechnol.* **4** 279–82

[30] Johnson W A and Warne L K 1995 Electrophysics of micromechanical comb actuators *J. Microelectromech. Syst.* **4** 49–59

[31] Wang K and Nguyen C T-C 1999 High-order medium frequency micromechanical electronic filters *J. Microelectromech. Syst.* **8** 534–57

[32] Adelung R, Aktas O C, Franc J, Biswas A, Kunz R, Elbahri M, Kanzow J, Schürmann U and Faupel F 2004 Strain-controlled growth of nanowires within thin-film cracks *Nat. Mater.* **3** 375–79

[33] Elbahri M, Rudra S K, Wille S, Jebril S, Scharnberg M, Paretkar D, Kunz R, Rui H, Biswas A and Adelung R 2006 Employing thin-film delamination for the formation of shadow masks for nanostructure fabrication *Adv. Mater.* **18** 1059–62

[34] Thurn J and Cook R F 2002 Stress hysteresis during thermal cycling of plasma-enhanced chemical vapor deposited silicon oxide films *J. Appl. Phys.* **91** 1988–92
[35] Mani S and Saif T 2007 Stress development in plasma-deposited silicon dioxide thin-films due to hydrogen evolution *Thin Solid Films* **515** 3120–5
[36] Mani S and Saif T M 2005 Mechanism of controlled crack formation in thin-film dielectrics *Appl. Phys. Lett.* **86** 201903
[37] Tang P T 1998 Fabrication of micro components by electrochemical deposition, part A *PhD Thesis* The Institute for Manufacturing Engineering (IPT), Technical University of Denmark (DTU)
[38] Tang P T 2001 Pulse reversal plating of nickel and nickel alloys for MEMS *Proc. SUR/FIN (Nashville)* pp 224–32
[39] Vedel T 1993 Termiske og mekaniske egenskaber af tynde metalliske belægninger *PhD Thesis* Technical University of Denmark (DTU) (in Danish)